THE EFFECT OF ASPECT RATIO ON COMPRESSOR PERFORMANCE

Ho-On To
Whittle Laboratory
University of Cambridge
hot20@cam.ac.uk

Robert J. Miller
Whittle Laboratory
University of Cambridge
rjm76@cam.ac.uk

ABSTRACT

It is shown that the optimum aspect ratio at which max efficiency occurs is relatively low, typically between 1 and 1.5. At these aspect ratios, inaccuracies inherently exist in the decomposition of the flow field into freestream and endwall components due to the absence of a clear freestream. In this paper, a unique approach is taken: a 'linear repeating stage' concept is used in conjunction with a novel way of defining the freestream flow. Through this unique approach, physically accurate decomposition of the flow field for aspect ratios as low as ~0.5 can be achieved.

This ability to accurately decompose the flow leads to several key findings. First, the endwall flow is found to be dependent on static pressure rise coefficient and endwall geometry, but independent of aspect ratio. Second, the commonly accepted relationship that endwall loss coefficient varies inversely with aspect ratio is shown to be physically inaccurate. Instead, a new term, which the authors refer to as the 'effective aspect ratio', should replace aspect ratio. It is shown that not doing so can result in efficiency errors of ~0.6% at low aspect ratios. Finally, there exists a low aspect ratio limit below which the two endwall flows interact causing a large separation to occur along the span. From these findings, a low order model is developed to model the effect of varying aspect ratio on compressor performance.

The last Section of the paper uses this low order model as well as a simple analytical model to show that to a first order, the optimum aspect ratio is just a function of the loss generated by the endwalls at zero clearance and the rate of change in profile loss due to blade thickness. This means that once the endwall configuration has been selected i.e. cantilever or shroud, the blade thickness sets the optimum aspect ratio.

INTRODUCTION

At any location in an axial compressor, for a fixed Mach number triangle and pitch-to-chord, there is an aspect ratio which achieves the maximum possible efficiency at the design condition. This aspect ratio may or may not result in the compressor achieving its desired operating range. However, in terms of design efficiency alone, the aspect ratio may be considered optimum. In practice, a designer may consider a number of reasons when setting the aspect ratio e.g mechanical, materials, achieving a desired

operating range or maximising design performance. Whatever their choice, it is important for them to understand how much their chosen aspect ratio differs from the optimum and what implications this has on performance.

The reason that an optimum aspect ratio exists can be seen in Fig. 1; the figure shows the variation in profile loss and endwall loss with aspect ratio. As the aspect ratio is increased, the optimum occurs at the point where the rate of increase in profile loss is equal to the rate of decrease in endwall loss. The figure also shows that for the design considered, the optimum aspect ratio is ~1.15. It will be shown in this paper that the optimum aspect ratio is typically below ~1.5, and will vary depending on the particular compressor stage considered.

The relatively low aspect ratio at which the optimum occurs makes it incredibly difficult to accurately predict the optimum. This is because at aspect ratios below ~1.5, no discernible freestream is observed in the compressor flow field, which makes attributing parts of the flow to either profile or endwall incredibly ambiguous. Since the optimum aspect ratio is set by the balance between profile and endwall loss, it is difficult to predict the optimum aspect ratio with any real certainty if it is below ~1.5.

This problem was recognised by Smith [1] whose response was to only decompose the flow for aspect ratios above ~2 i.e. compressors which exhibited clear freestream regions. The difficulty in decomposing the flow at low aspect ratios adds to the general confusion with regards to the optimum aspect ratio as reported by Wennerstrom [2].

This paper aims to bring clarity to the way in which the flow is decomposed, which in turn allows the effect of aspect ratio to be accurately predicted. Hence, the optimum aspect ratio can then be determined for a given compressor stage. The problem of accurate flow decomposition is tackled using simplifications proposed by McKenzie [3], and builds on the work by Smith [1]. This approach (described in detail later in the paper) results in an incredibly accurate and unambiguous decomposition of the flow down to aspect ratios as low as ~0.5.

In addition to design efficiency, the operating range of a compressor is believed to be strongly linked to its aspect ratio. This relates to the fact that many high aspect ratio compressors in the past were found to have poor operating range as reported by Wennerstrom [2]. Since steady RANS CFD with mixing planes is used in this paper, the true operating range of the compressor is therefore unlikely to be accurately predicted. However, a max pressure rise coefficient was observed in the CFD for all cases; this typically occurred when an endwall separation suddenly increased in size non-linearly, causing a dramatic increase in blockage. Hence, the max pressure rise coefficient is considered to be an indication of the operating range of the compressor, and can be correlated against various parameters akin to Koch [4]. When correlated in this way, the max pressure rise coefficient is found to depend largely on one particular parameter; this will be discussed in the final Section of the paper.

The design efficiency of a compressor is not just a function of AR, but is also dependent on a collection of non-dimensional parameters as shown in Eq. (1). (This equation reflects the way preliminary design systems typically predict efficiency.)

$$\eta = f\left(\phi_d, \psi_d, \Lambda_d, M_b, DF, AR, \frac{t}{c}, \frac{\varepsilon}{c}, Re_c, \text{config}\right) \quad (1)$$

In this paper, a number of simplifications have been made: the design Mach number triangles along with DF are all fixed ($\phi_d = 0.60$, $\psi_d = 0.44$, $\Lambda_d = 50\%$, $M_b = 0.1$, DF = 0.45). Eq. (1) then simplifies to Eq. (2).

$$\eta = f\left(AR, \frac{t}{c}, \frac{\varepsilon}{c}, Re_c, \text{config}\right) \quad (2)$$

Thus, the blade profile and pitch-to-chord are effectively fixed throughout the entirety of this paper; this allows the effect of aspect ratio to be studied in depth at a single point on the Smith Chart. The success of such a study will open up the opportunity to explore the Smith Chart in the future.

The paper is subsequently split into four Sections. In the first three Sections, a novel method of achieving accurate flow decomposition is presented, the decomposition is used to highlight various key findings, and finally, the improved knowledge of flow decomposition is used to develop a low order model capable of predicting the effect of aspect ratio on compressor performance. In the final Section of the paper, a number of specific questions are answered as follows:

1) **What does the optimum AR depend on?**

2) **How does the optimum AR vary across design space?**

3) **What are the underlying physical mechanisms which set the optimum AR?**

4) **Does achieving the optimum AR matter?**

1. PHYSICALLY ACCURATE FLOW DECOMPOSITION

The overall flow field through a compressor stage can be thought of as the superposition of two flow fields: a flow field associated with the profile alone and a flow field associated with the presence of the endwall. These flow fields will be referred to as the 'freestream flow' and the 'endwall flow' respectively. It will be shown that if the overall flow field is decomposed accurately into these two flow fields, then both flow fields are independent of AR down to values of ~0.7.

If the AR is low (typically less than ~1.5), defining the freestream flow becomes uncertain. This is because the hub and casing endwall flows interact at mid-height causing the flow to have no discernible freestream. An additional complication in defining the freestream flow is caused by the spanwise variation of the velocity triangles due to the hub-to-tip variation in blade speed.

In this paper, these problems have been solved by using the simplifications of the 'linear repeating stage' concept proposed by McKenzie [3], plus a novel way of defining the freestream flow. This means that the hub-to-tip ratio is effectively equal to one i.e. each blade-row is like a linear cascade, causing the freestream flow to be uniform along the span. In addition, the freestream flow is defined as the flow field which would exist if the profile alone (i.e. no endwalls) was operating at the same pressure rise coefficient as the overall flow field. (This is equivalent to the flow field present if the real stage had inviscid endwalls.) The endwall flow can then be determined by subtracting the freestream flow from the overall flow field.

Before demonstrating the accuracy of this method of flow decomposition, the repeating stage condition will now be presented. In addition, it should be noted that the flow throughout this paper is incompressible; this significantly aids the accuracy of loss decomposition by enabling the use of parallel endwalls, thus allowing the blade span to be constant through the stage. When considering the simplifications used, it should be remembered that the aim of this method is not to accurately predict real compressors, but to bring clarity and simplicity to the problem; thus allowing the underlying loss mechanisms to be examined.

Repeating stage condition

Smith [1] observed that by the third/fourth stage of a multistage compressor with repeating stages, the spanwise distributions of the flow had stopped deteriorating and had begun settling to an equilibrium. This behavior (referred to as the 'repeating stage condition') acts to couple the inlet boundary layer to the blade geometry, causing it to change in a natural way e.g. a change in endwall clearance size will cause the thickness and skew of the inlet boundary layer to also change. This means that the inlet boundary layer is not an input.

$$\frac{\delta^*}{c} = f\left(AR, \frac{\varepsilon}{c}, \frac{t}{c}, Re_c, \psi_b'\right) \quad (3)$$

For a 50% reaction cascade-like case with identical rotors and stators, the inlet boundary layer is then a function of the blade parameters and Re_c as shown in Eq. (3). (Note that the blade profile (as mentioned earlier) is effectively fixed throughout this paper; hence blade angles and pitch-to-chord are left out of Eq. (3).) The pressure rise coefficient (i.e. the particular point on the characteristic) also sets the inlet boundary layer thickness as will be shown in the next Section.

In order to model the repeating stage condition, a repeating stage model was implemented in steady CFD with mixing planes. (Details of this model will be presented in Section 3.) The basic idea is to start with a uniform inlet flow, converge the solution, and then feed the exit spanwise distributions back into the inlet before re-converging the solution. This can be repeated until the repeating stage condition is reached.

An example of the variation in lost efficiency with the number of repeating stage iterations can be seen in Fig. 2. (Note that the first iteration represents a stage with a uniform inlet.) The figure shows that the lost efficiency rises sharply to begin with, changing by 0.6% over the first three repeats, but then begins to approach an asymptote and only changes by ~0.3% over the next seven repeats.

Since the efficiency of the stage approaches an asymptote, it is expected that the inlet boundary layer must settle to an equilibrium. One way of visualising this is by plotting the development of the spanwise whirl angle distribution at stage exit; this can be seen in Fig. 3. The figure shows that by the third repeating stage iteration, the whirl angle distribution is already similar in shape to that of the tenth iteration.

It is important to remember that the purpose of this method is not to achieve an exact repeating stage condition, but instead to ensure that the inlet profile is representative of an embedded stage. Therefore, ten repeating stage iterations was considered to be adequate and chosen to generate the CFD results throughout the entirety of this paper.

Demonstration of accurate flow decomposition

To demonstrate the accuracy of the flow decomposition, an example will be shown with AR varying from 3.5 down to 0.5.

The first case considered has a relatively high AR of 1.7, a case which exhibits a clear freestream. Entropy plots at rotor inlet and exit for this case can be seen in Fig. 4. The figure also shows various endwall flow features typically found in compressor flows: a closed corner separation at the hub as well as tip leakage flow at the casing. (Note that the inlet is circumferentially uniform due to the use of mixing planes.)

The effects of endwall loss can be more clearly observed by removing the effect of the inlet boundary layer. This has been achieved by plotting the local change in entropy, which has been non-dimensionalised as a local loss coefficient as shown in Fig. 5a). Care should be taken when interpreting this figure as calculation of the overall blade loss coefficient would require the inlet and exit entropy to be first appropriately averaged, before subtracting one from the other.

In Fig. 5a), non-zero values either result from loss (positive values) or distortion of the inlet boundary layer as it passes through the blade-row (positive and negative values). (N.B.: Ideally, the inlet boundary layer distortion effect would have been removed from the plots. However, this requires stream tube tracking through the solution which is difficult and prone to error.)

Fig. 5b) shows the case for the freestream flow (i.e. the same compressor run with inviscid endwalls operating at the same pressure rise coefficient). Fig. 5c), which is the result of subtracting Fig. 5b) from Fig. 5a), represents the endwall flow. The structure of the endwall flow can be considered to be in two parts. Close to the endwall, the endwall secondary flows, corner separations and

leakage flows are observed. Further from the endwall, there is a region away from the traditional endwall flow features which is caused by the inlet boundary layer distorting the freesteam flow.

To see how the decomposition of the flow changes with ARs below 1.5 i.e. cases with no discernible freestream, a case with an AR of 0.7 is shown in Fig. 6. The figure shows the absence of a clear freestream, the cause of which can be seen to be the merging of the hub and casing endwall regions arising from the distortion of profile loss by the inlet boundary. It is important to note that at this AR, the hub and casing endwall secondary flows have still not started to interact. The fact that the endwall flows remain unchanged from the previous case (Fig. 6c) implies that even down to an AR of 0.7, the endwall flow (and hence, the loss generated by the endwalls) is independent of AR.

To confirm this hypothesis that the flow field associated with the presence of the endwalls is independent of AR, the variation in loss generated by the endwalls (i.e. the total loss less the "freestream" loss) with AR can be seen in Fig. 7. The figure shows that the loss generated by the endwalls is independent of AR down to values of ~0.5. This demonstrates that by using the 'linear repeating stage' concept plus an alternative way of defining the freestream flow, the overall flow field can be decomposed into freestream and endwall flows in such a way that both flow fields become independent of AR down to values of ~0.5. Hence, the decomposition can be considered to be physically accurate.

2. KEY FINDINGS FROM FLOW DECOMPOSITION

The physically accurate decomposition of the flow field has revealed a number of key findings about how freestream and endwall flows 'communicate'.

Endwall flow independence of AR

Fig. 8 shows the characteristics of three compressors with very different ARs. (The horizontal shift in the characteristics shall shortly be explained.) Contours of local flow coefficient in the endwall separation region are shown at two pressure rise coefficients. It is important to note that the axes of the contour plots have been non-dimensionalised with chord.

There are two points of interest with regards to the contour plots shown in Fig. 8. First, at any fixed pressure rise coefficient, the endwall flow contours at all ARs are identical. This confirms that the endwall flow is independent of AR (as discussed in the previous Section). Second, and rather more surprisingly, the endwall flow contours over the whole characteristic exhibit the same pattern but are of a different size/depth depending on the pressure rise coefficient. The figure shows that the endwall flow contours at the max pressure rise coefficient look like a photographic scale of the endwall flow contours at the lower pressure rise coefficient.

In addition, since the max pressure rise coefficient is set by the endwall flow, the max pressure rise coefficient must also be independent of AR as shown by the dashed horizontal line in Fig. 8. This is in agreement with the concept proposed by Smith [1] and Koch [4].

Because the endwall flow appears to be set by the pressure rise coefficient, one would expect that the ratio of blockage-to-chord is a function of pressure rise coefficient (and not AR). To demonstrate this, the blockage-to-span can be calculated using Eq. **(**4**)**; it is set by the flow coefficient of the freestream flow and the mean flow coefficient of the overall flow field. (Note that this definition of blockage accounts for both endwalls, and is analogous to the displacement thickness used in external aerofoils.) The freestream flow coefficient which needs to be used is the flow coefficient associated with the "freestream" flow as defined earlier in Fig. 6b).

$$\frac{\delta^*}{h} = 1 - \frac{\phi_{mean}}{\phi_{fs}} \tag{4}$$

$$where \quad \phi_{mean} = \frac{\dot{m}}{\rho A U} \quad \& \quad \phi_{fs} = \frac{V_{x,fs}}{U}$$

Multiplying blockage-to-span by AR gives blockage-to-chord; this is plotted in Fig. 9 against the blade-row pressure rise coefficient. The red symbols on the figure clearly confirms that blockage-to-chord is set by the pressure rise coefficient and is independent of AR.

It is important to note that if ϕ_{fs} is set equal to the mid-height flow coefficient (a method traditionally used even when no clear freestream exists) instead of using the "freestream" flow definition of Fig. 6b), the blockage-to-chord will not appear to be independent of AR. This can be seen in Fig. 9 for the AR = 0.86 case as shown by the grey crosses.

Fig. 9 also helps to explain the horizontal shift in the characteristics as mentioned earlier in Fig. 8. Since the same blade profile is used for all ARs, the three cases in Fig. 8 must therefore have the same freestream characteristic. In addition, at a given pressure rise coefficient, the blockage-to-chord is the same for all three cases. Hence, the horizontal shift is caused by the difference in blockage-to-span due to the differing ARs. As the pressure rise coefficient increases, the blockage-to-chord also increases causing a larger horizontal shift from the freestream characteristic at lower ARs. Thus, characteristics of low AR stages roll over more than high AR stages. This effect was previously observed by Smith [1].

Effective aspect ratio

The endwall loss coefficient is typically considered to vary inversely with AR. However, this relationship was found to be inaccurate especially at low ARs. Instead, the endwall loss coefficient was found to vary inversely with a new term referred to as the 'effective AR'; this is defined in Eq. (5).

$$AR_{eff} = AR\left(1 - {\delta^*}/{h}\right) \quad or \quad \frac{h - \delta^*}{c} \tag{5}$$

The physical reason that effective AR is required is because the total mass flow through a compressor scales with the effective span i.e. $h - \delta^*$, while the mass flow influenced by the endwall flow scales with chord (as implied by Fig. 9). By definition, the endwall loss coefficient is inversely proportional to the ratio of these two quantities; hence, the authors have decided to refer to this ratio as the 'effective AR'.

In order to show this in CFD, the endwall loss coefficient can be calculated using Eq. (6). Once again, it is important to recognise that the freestream quantities used in the total and profile loss coefficients must be associated with the "freestream" flow as defined earlier in Fig. 6b). (Note that this endwall loss coefficient is a blade-row quantity i.e. includes both endwalls.)

$$\omega_{ew} = \omega_t - \omega_p \tag{6}$$

$$where \quad \omega_t = \frac{T\Delta s}{\frac{1}{2}V_{fs}^2} \quad \& \quad \omega_p = \frac{T\Delta s_{fs}}{\frac{1}{2}V_{fs}^2}$$

Fig. 10 shows the endwall loss coefficient multiplied by both AR (grey symbols) and AR_{eff} (red symbols) plotted against pressure rise coefficient for three different ARs. Since the red symbols collapse onto a single curve whereas the grey symbols do not, this implies that the endwall loss coefficient is inversely proportional to the effective AR and not just AR. There is no reason why this is not also true in turbines.

Using the low order model described in the next Section, it can be shown that using AR instead of effective AR leads to the stage efficiency being overpredicted by ~0.6% for AR = 0.7 and ε/c = 1%. This discrepancy means that it is important for preliminary design systems to use effective AR especially when ARs are very low e.g. rear stages of high pressure compressors.

Low aspect ratio limit

Fig. 11 is similar in form to Fig. 7; however, the vertical axis is now endwall loss coefficient multiplied by effective AR. In addition, blockage-to-chord has also been plotted on the secondary axis.

As the AR is reduced from 0.7 to 0.5, a slight reduction in the endwall loss and blockage is observed. This region (labelled as 'potential flow interaction' in Fig. 11) is caused by the potential fields associated with the hub and casing endwall flows interacting with each other. Effectively, the hub and casing endwall flows appear to suppress the size of each other. It is also observed that the change in blockage is more dramatic than loss, with a reduction of ~15%.

Below an AR of ~0.5, the two inner endwall regions (i.e. the regions labelled 'endwall loss' in Fig. 5) meet, resulting in flow separation along the whole span. At this point, the compressor cannot reach the design pressure rise coefficient; hence, values below this AR are not plotted on the figure.

3. LOW ORDER MODEL DEVELOPED

Based on the physical understanding developed in the previous Sections, this Section describes the formulation of a low order model which is used to model the effect of AR on performance. More specifically, it models the effect of AR, ε/c, t/c, and Re_c on a stage with the following design values: $\phi_d = 0.60$, $\psi_d = 0.44$, $\Lambda_d = 50\%$, $M_b = 0.1$ and DF = 0.45. This Section is split into four parts: the model structure, the CFD setup used to explore the parameter space, correlations used in the model, and validation of the model.

The reader should note that the model is not aimed at accurately predicting real compressors; instead, its aim is to bring clarity to the fundamental effect of AR by using simplifications akin to Smith [1] and McKenzie [3]. The benefit of the model over the CFD (on which it is based) is the low order physical understanding it provides. The absolute accuracy of the model will be revisited at the end of the paper.

Model structure

The structure of the model is relatively simple and is shown in Fig. 12. (Note that this procedure must be done for both rotor and stator.) First, the blade parameters i.e. AR, ε/c, t/c, and Re_c must be specified. The freestream flow coefficient is then inputted; this sets the pressure rise coefficient which in turn sets the endwall flow and blockage (as described earlier in Figs. 8 & 9). Once the blockage is determined, the mean flow coefficient and the effective AR can both be calculated. Both profile and endwall loss coefficients can then be determined; hence, the efficiency can finally be predicted. In order to generate a characteristic, this procedure is repeated at different freestream flow coefficients until the max pressure rise coefficient is reached. This max pressure rise coefficient is determined from a correlation based on the blade parameters (but not AR as discussed earlier in Fig. 8) akin to Koch [4]. Before the correlations used in the model are shown, the CFD setup used to develop these correlations will now be presented.

CFD setup

The CFD solver used was a RANS code with a Spalart-Allmaras turbulence model [5]. All CFD runs were steady with mixing planes between blade-rows. The solutions were undertaken on a three blade-row single-passage domain; rotor, stator, rotor. Once convergence was achieved, the stator exit conditions were taken as the inlet condition for the next solution. In all cases, this process was repeated ten times. The repeating stage solution is considered to be the tenth solution.

The number of cells per blade-row was ~10^6 and the fully meshed shroud cavity also had ~10^6 cells; the number of points axially and radially across each seal tooth in the shroud cavity were ~20 and 30 respectively. (It is worth noting that the exact number of cells was dependent on the blade parameters e.g. AR, cantilever clearance size, shroud clearance size.) The fraction of total mass flow passing through the cavity was comparable to the experimental results of Wellborn [6].

The blade parameters (ε/c, t/c and Re_c) were varied independently and CFD was run over the whole characteristic. The total number of solutions undertaken around this parameter space was ~400 over approximately the following ranges: AR = 0.8-3.4, ε/c = 0-4%, t/c = 2-8%, Re_c = 10^5-10^6.

The blade profile used is representative of a modern controlled diffusion-style aerofoil. No 3D design i.e. no lean or sweep was applied, and the blade profile was uniform along the span as explained earlier. The blade was re-cambered as necessary for two reasons: to achieve the required exit flow angle and to achieve the 'smooth flow condition' at the design pressure rise. The 'smooth flow condition', which occurs when the stagnation point coincides with the nose of the aerofoil (Smith [1]), was chosen to ensure consistency between cases. (Note that since the design Mach no. triangles and DF are fixed, only small amounts of re-cambering were required.)

In order to investigate the different effect of cantilevered and shrouded endwalls, the hub and casing endwalls were set to be identical; the two cases considered are shown in Fig. 13. It is clear that the shrouded case of Fig. 13b) does not currently exist in reality. However, it brings anti-symmetry to the problem, thus allowing the effect of cantilevered and shrouded endwalls to be decoupled from each other. If the endwall configuration of a real shrouded compressor was used, the hub and casing endwalls would have different max pressure rise coefficients, thus making it difficult to decouple the endwalls.

Correlations

A selection of the key correlations used in the model will now be presented.

Fig. 14 shows the variation in endwall loss coefficient for cantilevered endwalls with clearance-to-chord and pressure rise coefficient. The raw data has been included to demonstrate the accuracy of the flow decomposition at all clearance-to-chords and pressure rise coefficients.

Fig. 15 compares the loss generated by cantilevered and shrouded endwalls. There are two points to note from the figure: First, for the same clearance-to-chord, cantilevered endwalls generate ~10-20% lower loss than shrouded endwalls at typical clearance-to-chords. Second, also for the same clearance-to-chord, the max pressure rise coefficient of the cantilever is higher than that of the shroud. These findings are somewhat unexpected as they disagree with the concept of a 'cross-over' clearance size proposed by

Freeman [7] at which the relative merits of cantilever and shroud swop over. It is worth noting that the max pressure rise coefficient even at the smaller clearances do not extend much beyond the design pressure rise coefficient; it is not known exactly why this is the case although 3D blade design and unsteady CFD are likely to significantly increase the predicted max pressure rise coefficients.

In order to determine the actual endwall loss coefficient for cantilevered and shrouded endwalls, the effective AR must be calculated; therefore, the blockage must be known. Fig. 16 shows the variation in blockage-to-chord for cantilevered and shrouded endwalls. An interesting feature of the figure is that as the pressure rise coefficient increases, the rate of increase of blockage for shrouded endwalls is much greater than for cantilevered endwalls. (This might be because cantilevered clearance flows suppress endwall separations by re-energising the low momentum endwall flow.) This in turn causes the slope of shrouded compressor characteristics to 'roll over' more towards stall than their cantilevered counterparts; this phenomenon has been observed experimentally (Wellborn [6]).

Another important point of interest is that blockage is not a good indicator of loss. Consider ε/c = 1% at the design pressure rise coefficient; Fig. 16 shows that the blockage is ~25% higher for cantilevered endwalls than for shrouded endwalls, yet Fig. 15 shows that the loss generated by cantilevered endwalls is ~15% lower than for shrouded endwalls.

Fig. 17 shows the effect of blade thickness on profile loss using the coupled Euler/boundary layer code, MISES (Drela [8]). It must be noted that in this study, LE, TE and max thicknesses all scale together. The figure shows that the rise in profile loss is approximately linear with thickness-to-chord with a theoretical zero thickness profile loss of ~1.4%. This rise is due to two loss mechanisms: the first is the increase in the BL edge velocities which causes a rise in entropy generation (since this is proportional to the BL edge velocity cubed). The second is an increase in wake mixing loss, which is roughly proportional to the TE thickness-to-chord.

In an attempt to decouple the two mechanisms, the LE & max thicknesses-to-chord were varied together without varying TE thickness-to-chord. This was found to be responsible for ~40% of the increase in profile loss. Hence, by deduction, the other ~60% increase can be assumed to be due to the effect of TE thickness-to-chord.

Fig. 18 shows the effect of Re_c on profile loss in MISES, which can be run with fully turbulent BLs or a transition model. The correlation of Wright & Miller [9] is also plotted and shows a traditional view of three Reynolds number regions: laminar, turbulent, and hydraulically rough.

MISES and Wright & Miller's correlation seem to show reasonable agreement. The difference between the transitional and fully turbulent MISES solutions shows that even though the Wright & Miller correlation correctly predicts the shape of the graph, the

physical causes of this shape are wrongly prescribed, with turbulent flow existing over most of the profile even below $Re_c = 10^5$ and laminar flow existing even at $Re_c \sim 10^6$.

Fig. 19 shows a comparison of the effect of Re_c on profile and endwall losses. It is interesting to note that the dependence of endwall loss on Re_c is weaker than for profile loss. This is because while attached loss varies with $\sim Re_c^{-0.2}$, mixing losses away from solid surfaces are more or less independent of Re_c.

In this particular case, endwall loss is a weaker function of Re_c because of the larger proportion of mixing loss in endwall loss than in profile loss. How much weaker this function is will depend on ε/c.

Validation

To validate the low order model, a datum test case (AR = 0.86) with a shrouded stator was created and is representative of a rear stage in a modern HP compressor. Note that this datum test case has identical rotors and stators, with the only difference in the blade-rows due to the stator being shrouded and the rotor being cantilevered. The specification of the stage is shown in Table 1. The stage was then run in CFD using the repeating stage model described earlier, with the resulting performance shown by the red lines in Fig. 20.

Based on Fig. 15 (which suggested that cantilevered endwalls generate lower loss than shrouded endwalls), the stator was switched from shrouded to cantilevered. The AR was then optimised using the low order model by assuming that the absolute clearances and blade thicknesses are fixed. The optimum stage was found to have an AR of 1.16, and its performance as predicted by the low order model is shown by the dashed blue lines in Fig. 20. This new design was then run in CFD and the blade profile was re-cambered such that the design point was closer to the datum; the performance of this design in CFD is shown by the solid blue lines in Fig. 20.

A comparison between the blue dashed and solid lines in Fig. 20 shows excellent agreement between the low order model and the CFD. The model not only accurately predicts the characteristic and stage efficiency, but also the max pressure rise coefficient. (Note that if the optimum case was redesigned so that its design point exactly passed through the design point of the datum, the whole characteristic would essentially slide downwards and the agreement in the max pressure rise coefficient would appear to be even better.)

The low order model suggests that the optimum compressor efficiency is 0.57% higher than the datum. Interestingly, 0.39% of this efficiency gain is due to switching from a shrouded stator to a cantilevered stator; the remaining 0.18% is from optimising the AR of the stage. The underlying physical mechanisms which set the optimum AR will be discussed in the next Section.

4. QUESTIONS

The aim now turns to answering the questions defined in the introduction by using the low order model developed in the previous Section. Before answering these questions, it is important to reiterate/emphasise the assumptions used in this Section. First, it should be reminded that the design Mach number triangles and DF are fixed ($\phi_d = 0.60$, $\psi_d = 0.44$, $\Lambda_d = 50\%$, $M_b = 0.1$, DF = 0.45). Second, if the mass flow, pressure, temperature, and radius are all set, then the span is fixed; hence AR is varied by varying chord length. Third, mechanical constraints are assumed to exist such that the absolute clearances and blade thicknesses (which includes LE, TE and max thicknesses) are assumed to be fixed. This means that as AR is varied, clearance-to-chord and thickness-to-chord also vary. Finally, it is assumed that the axial gaps between blade-rows scale with chord. (In reality, this final assumption may prove to be the least valid but it is necessary to simplify the problem into a manageable one.)

To aid answering the questions posed in the introduction, the lost efficiency has been broken down into four loss sources using the low order model as shown in Fig. 21. Furthermore, the profile loss has subsequently been broken down into two: the 'profile loss at zero thickness' i.e. the theoretical profile loss achieved by a zero thickness blade, and the 'profile loss due to thickness'. Similarly, the endwall loss has also been broken down into two: the 'endwall loss at zero clearance' i.e. the theoretical endwall loss attained if the clearance was zero, and the 'endwall loss due to the clearance'. In the remainder of this Section, these four loss sources will be used to aid physical interpretation.

What does the optimum AR depend on?

Considering that the blade profile is fixed, it is intuitive to assume that the optimum AR is a function of the following three non-dimensionals and endwall configuration as shown in Eq. (7).

$$AR_{opt} = f\left(\frac{t}{c}, \frac{\varepsilon}{c}, Re_c, \text{config}\right) \quad (7)$$

However, if the absolute blade thickness and clearance are fixed, varying AR by varying chord causes all three non-dimensionals to vary. Therefore, the relationship above is of little use to the designer if he/she wants to estimate the optimum AR at the start of the design process.

The alternative is to use span as the length scale for non-dimensionalisation, since the span will remain constant as the chord is varied. This gives the following relationship shown in Eq. (8).

$$AR_{opt} = f\left(\frac{t}{h}, \frac{\varepsilon}{h}, Re_h, \text{config}\right) \quad (8)$$

The first and second parameters are straight forward geometric parameters. The third parameter, Reynolds number based on span, is a little subtler. Conventionally, the Reynolds number is based on chord and is a measure of the ratio of inertial to viscous forces over the particular blade profile. The Reynolds number based on span is a measure of the ratio of inertial to viscous forces in the annulus as a whole. It is analogous to the Reynolds number based on diameter used in pipe flow.

Re_h in a real machine is fixed by the mass flow, radius and stage inlet dynamic viscosity. The mass flow is constant and the radius is roughly constant through a particular compressor spool. This means that the only parameter which affects Re_h is the dynamic viscosity which in turn is affected by temperature. In a high pressure core of a large civil turbofan engine, Re_h may typically vary from around 5×10^5 to 1×10^6; this is roughly the range which has been selected in this study.

It should be noted that in preliminary design i.e. before blades have been designed, the three dimensionless parameters in the equation above are all known; thus the optimum AR can be estimated at the very start of the design process.

How does optimum AR vary across design space?

The three dimensional design space for optimum AR, for a cantilevered compressor, derived using the model, is summarised in Figs. 22 & 23. Fig. 22 shows a slice through the space at constant Re_h = 5.5x10^5 whereas Fig. 23 shows a slice through the space at constant ε/h = 1.2%. In addition to contours of optimum AR, both figures also show contours of efficiency and ε/c. The reason for including ε/c is that later in the Section, it will be shown that there is a strong correlation between max pressure rise coefficient and ε/c; hence, ε/c gives a measure of operating range.

Figs. 22 & 23 show that over most of the design space, the optimum AR is a strong function of t/h, and a weak function of ε/h and Re_h. The reason for this may not be immediately clear, but will be discussed in more depth later in this Section.

It can be seen on Fig. 22 that at higher values of ε/h, the contours of optimum AR curve downwards. This is because as ε/h increases, the max pressure rise coefficient decreases for a fixed AR. At the point where the max pressure rise coefficient is equal to the design pressure rise coefficient, the optimum AR is then set by this condition. (Note that if the max pressure rise coefficient was always very large, then the contours of optimum AR would continue to be approximately horizontal.)

As Re_h decreases (or Re_c decreases for a fixed AR), the rate of increase in loss becomes greater. (This can be seen in Fig. 18 from the previous Section.) This effectively reduces the optimum AR which results in the slight curve downwards at low Re_h on Fig. 23.

The lines of constant efficiency behave very predictably; the efficiency drops approximately linearly with increasing ε/h and t/h. A decrease in Re_h causes a reduction in efficiency, with a sharper reduction occurring at lower Re_h.

A comparison of the optimum AR for the endwall configurations of Fig. 13 is shown in Fig. 24. For clarity, only the ε/h = 0% case is shown and the optimum AR is plotted against t/h. (This removes the additional effect of clearance which complicates the problem as will be shortly explained.) The figure shows that shrouded configurations have a slightly higher optimum AR than cantilevered configurations. However, the figure also shows that this difference is relatively small: less than 5% difference. It is worth noting that the red curve in Fig. 24 is the optimum AR for the shrouded configuration of Fig. 13b). Hence, the optimum AR for a real shrouded compressor (i.e. shrouded stator only) will lie somewhere between the red and blue curves in the figure. (The shrouded configuration of Fig. 13b) was used to maintain anti-symmetry as explained in the previous Section.)

In addition to affecting design efficiency, the choice of AR also affects the operating range. In fact, many attempts at designing high AR compressors in the past were not successful due to their lack of operating range (Wennerstrom [2]). As discussed in the introduction, the CFD is unlikely to be accurate at predicting operating range. However, in all the CFD results obtained, the max pressure rise coefficient was physical; it occurred when an endwall separation (and hence blockage) increased rapidly in size akin to Smith [1]. The max pressure rise coefficient is therefore used in this study as a measure of the operating range.

The relationship between operating range and AR is observed to be relatively simple. In the low order model presented in the previous Section, the max pressure rise coefficient across a blade-row, $\psi'_{b,max}$, is correlated with the three dimensionless parameters: ε/c, t/c and Re_c. Fig. 25 clearly shows that ε/c is responsible for most of the change in max pressure rise coefficient for the case considered. If the designer has in mind a particular ε/c he/she does not want to exceed, he/she can look up ε/c on Figs. 22 & 23 to see whether the optimum AR causes ε/c to exceed this limit. If so, then the AR must be set based on this ε/c limit (rather than based on max efficiency).

What are the underlying physical mechanisms which set the optimum AR?

Fig. 21 shows that the loss sources which are strongly dependent on AR are the 'profile loss due to thickness' and the 'endwall loss at zero clearance'. Hence, it is these two loss sources which predominantly set the optimum AR. As the AR is increased, the thickness-to-chord increases causing an increase in the 'profile loss due to thickness'. At the same, the size of the endwall flow relative to the total flow decreases; this causes the 'endwall loss at zero clearance' to decrease, varying approximately inversely with AR. Thus, the optimum AR occurs when the rate of increase in one loss source balances the rate of decrease in the other loss source.

The other two loss sources in Fig. 21 i.e. the 'profile loss at zero thickness' and the 'endwall loss due to clearance', are both approximately constant with AR. Hence, these loss sources play a secondary role in setting the optimum AR.

Physical understanding of the optimum AR can be aided with a simple analytical model based on a few simple equations to model loss. These equations will now be described. To achieve this, a number of further simplifications have been made. First, the actual AR is used and not the effective AR; the impact of this on accuracy will be shortly discussed. Second, both profile loss and endwall loss coefficients are assumed to vary with Re_c^{-n}.

The total loss coefficient is the sum of the profile and endwall loss coefficients as shown in Eq. (9).

$$\omega_t = \omega_p + \omega_{ew} \tag{9}$$

It was shown earlier (Fig. 17) that the increase in profile loss with t/c is approximately linear. This results in the following expression for profile loss shown in Eq. (10).

$$\omega_p = \left(\omega_{po} + k_p \cdot \frac{t}{c}\right) \cdot k \cdot Re_c^{-n} \tag{10}$$

ω_{po} is the hypothetical profile loss at zero thickness (at a reference Re_c). The two constants ω_{po} and k_p can be estimated from Fig. 17.

Since the curves in Fig. 15 for cantilevered endwalls are fairly evenly spaced, this implies that the rise in the loss generated by the endwalls with ε/c is approximately linear. (This is less so for shrouded endwalls as shown by the blue curves in Fig. 15.) This results in the following expression for endwall loss shown in Eq. (11).

$$\omega_{ew} \times AR = \left(\zeta_{ewo} + k_{ew} \cdot \frac{\varepsilon}{c}\right) \cdot k \cdot Re_c^{-n} \tag{11}$$

ζ_{ewo} is the loss generated by the endwalls at zero clearance (at a reference Re_c). The two constants ζ_{ewo} and k_{ew} can be estimated from Fig. 15.

Rewriting Eq. (10) and Eq. (11) in terms of Re_h and substituting into Eq. (9) gives Eq. (12).

$$\omega_t = \left[k_p \cdot \frac{t}{h} \cdot AR^{n+1} + \left(\omega_{po} + k_{ew} \cdot \frac{\varepsilon}{h}\right) \cdot AR^n + \zeta_{ewo} \cdot AR^{n-1}\right] \cdot k \cdot Re_h^{-n} \tag{12}$$

For a fixed pressure rise coefficient, the total loss coefficient obtained from Eq. (12) can be used to calculate the lost efficiency. This is plotted against AR in Fig. 26 for the same case considered in Fig. 21.

A comparison between Figs. 21 & 26 shows very good agreement between the simple analytical model and the low order model in terms of the shape of the graph and the breakdown in loss sources. There are however a number of small differences between the two.

First, at ARs above the optimum, the rate of increase in loss is smaller for the simple analytical model. This is largely due to the thickness-to-chord effect on profile loss not being captured accurately enough. This relationship is not exactly linear as assumed by the simple analytical model; in fact, the gradient in Fig. 17 can be seen to increase slightly as thickness-to-chord increases.

Second, the simple analytical model predicts an optimum lost efficiency which is ~0.6% lower than the low order model. This is largely caused by the use of AR instead of effective AR. This highlights the importance of effective AR in accurately predicting loss especially at low ARs. Eq. (12) could potentially be improved to include this effect although the simple analytical model would not be so simple any more since a blockage correlation would be required. (This is because varying AR varies ε/c, t/c, and Re_c, which in turn cause blockage to change.) Hence, the authors consider the physical insight offered by the simplicity outweighs any potential improvements in absolute levels of accuracy.

Third, at ARs below the optimum, the rate of increase of 'endwall loss at zero clearance' is somewhat lower for the simple analytical model. Once again, this is due to using AR instead of effective AR. This means that even if thickness, clearance, and Re_c effects could all be modelled perfectly by the simple analytical model, it would still get the gradient of 'endwall loss at zero clearance' wrong. As a consequence, the optimum AR predicted by the simple analytical model would be too small. This is probably why the optimum AR from the simple analytical model (Fig. 26) is 1.07 and the optimum AR for the low order model (Fig. 21) is 1.15.

Eq. (12) can be used to analytically estimate the optimum AR. Differentiating Eq. (12), setting it equal to zero, and solving the resulting quadratic equation gives Eq. **Error! Reference source not found.**).

$$AR_{opt} \approx \sqrt{\frac{1-n}{n+1}\left(\frac{\zeta_{ewo}}{k_p \cdot \frac{t}{h}}\right)} + \frac{n}{2(n+1)} \cdot \left(\frac{\omega_{po} + k_{ew} \cdot \frac{\varepsilon}{h}}{k_p \cdot \frac{t}{h}}\right) \tag{13}$$

In most cases, the first term in Eq. **Error! Reference source not found.** is ~4 times greater than the second term. This implies that the loss generated by the endwalls at zero clearance, ζ_{ewo}, the rate of increase in profile loss due to blade thickness, $k_p \cdot \frac{t}{h}$, and the Reynolds number dependency, n, are the biggest factors which influence the optimum AR. For the case of cantilevered and shrouded compressors with zero clearance, the only parameter in Eq. **Error! Reference source not found.** which is different is ζ_{ewo}. Hence, the slightly higher value of ζ_{ewo} for shrouded endwalls causes the slightly higher optimum AR as shown earlier in Fig. 24.

It is worth noting that if n = 0, which is typically used in low order models when roughness becomes significant (see Fig. 18), the second term in Eq. **Error! Reference source not found.** is zero and this results in the simple expression of Eq. (14).

$$AR_{opt} \approx \sqrt{\left(\frac{\zeta_{ewo}}{k_p \cdot \frac{t}{h}}\right)} \qquad \text{for n = 0} \qquad \textbf{(14)}$$

This further emphasies the fact that over most of the design space, the optimum AR is predominantly a function of t/h (as shown in Figs. 22 & 23. This is also consistent with the fact that the losses most sensitive to AR are the 'profile loss due to thickness' and the 'endwall loss at zero clearance' (Figs. 21 & 26). Hence, it is the rate of change with AR of these two loss sources that largely sets the optimum AR.

Does achieving the optimum AR matter?

Fig. 27 not only shows the variation of optimum AR with t/h (blue line), but also shows the maximum and minimum ARs at which the efficiency is within 0.1% of the optimum. Therefore, any design within the area enclosed by the dashed lines achieves an efficiency of within 0.1% of the optimum. The graph shows a surprisingly wide range of acceptable ARs if the designer were to design within this area, ~±20% of the optimum AR. For t/h = 0.02, the permissible range of ARs is ~1.3 to 1.9, while for t/h = 0.07 the permissible range is ~0.78 to 1.14.

Another point to note is that every blade-row on a compressor spool is likely to have its own value of t/h (due to annulus contraction and mechanical constraints); this means that Fig. 27 could be used to estimate the optimum AR of every blade-row. This demonstrates the power of such a simple graph.

The accuracy with which the true optimum AR is known is also of interest. This study has been undertaken using CFD and therefore, there may be errors in the optimum AR stated in this paper when compared with the optimum for an experiment. This is an important question for designers as the losses in real engines may differ significantly from idealised cases.

A reasonably accurate estimate of the certainty with which optimum AR is known can be determined using Eq. (14). To a first order, the accuracy with which the true optimum AR is known depends only on the accuracy of the loss generated by the endwalls at zero clearance, ζ_{ewo}, and the rate of increase in profile loss due to thickness, $k_p \cdot \frac{t}{h}$.

The rate of increase in profile loss due to thickness can be determined relatively accurately using codes such as MISES and by making measurements in either cascades or rotating facilities. The uncertainty in this can be considered to be ~10%. The loss generated by the endwalls at zero clearance is much more difficult to determine. The accuracy of RANS codes in predicting endwall loss in a repeating stage environment is unclear. It is worth noting that transition may also have a significant effect on the loss generated by the endwalls at zero clearance (Goodhand [10]) and it is unlikely that existing RANS codes can predict transition reliably. Experiments are of course considered to be more reliable; hence, numerous experiments in the past have been undertaken in

large low speed multistage rigs. However, accurate flow decomposition of experimental data is exceptionally difficult especially at low ARs (as was discussed in Sections 1 & 2). The authors roughly estimate the uncertainty in the loss generated by the endwalls at zero clearance to be ~20%.

Considering these uncertainties and using Eq. (14), the uncertainty in our knowledge of the optimum AR is ~±15%. Although this estimation of uncertainty maybe rough, it shows that the uncertainty with which current experimental techniques/methods can determine the optimum AR is similar in magnitude to the variation of AR which results in a 0.1% change in efficiency. Therefore, improvements in experimental techniques/methods are crucial if the real optimum AR is to be accurately determined.

5. CONCLUSIONS

Considerable debate exists around the effect of AR on design efficiency. Thoughts vary widely from those who consider high aspect to offer the potential to improve performance (like with external wings), to those who consider low AR stages to have better performance. This study shows that some of this confusion is due to the inability to accurately decompose the flow field at low AR (<1.5).

A unique approach to decomposing the flow field into freestream and endwall flows has been developed by using the simplifications of the 'linear repeating stage' concept proposed by McKenzie [3] and a novel way of defining the freestream flow. The approach has been demonstrated to accurately decompose the flow down to an AR of ~0.7.

Four AR regions have approximately been determined. For AR>1.5, a clear freestream exists and the endwall flow was found to be independent of AR. For 0.7<AR<1.5, no clear freestream exists but the endwall flow was still found to be independent of AR. For 0.5<AR<0.7, the endwall flows interact causing their size to reduce slightly. And finally, for AR<0.5, the two endwall separations meet causing a full span separation to occur along the blade.

The commonly accepted relationship of endwall loss coefficient varying inversely with AR is inaccurate. Instead, a new term referred to as 'effective aspect ratio', should replace aspect ratio. It is shown that not doing so can result in efficiency errors of ~0.6% at low ARs.

The optimum AR was found to be surprisingly low over most of the design space varying from ~1 to 1.5. To a first order, the optimum AR was found to be set by two terms: the loss generated by the endwalls at zero clearance and the rate of increase in profile loss due to blade thickness.

Comparing cantilever and shrouded compressors showed the surprising result that this choice marginally affects the optimum AR by less than 0.1. However, it was also found that for existing technologies, switching from a shrouded stator to cantilevered stator increased efficiency by ~0.4%. Further work needs to be done to investigate whether or not this is true for a real compressor.

Finally, it has been shown that the range of ARs which will get the designer within 0.1% efficiency of the optimum is relatively wide. This range of ARs is typically ±20%. This gives the designer the freedom to optimise for other parameters such as weight, mechanical, or thermal limits while still achieving a performance close to the optimum.

ACKNOWLEDGEMENTS

The authors would like to thank Nick Cumpsty, Chris Freeman, Simon Gallimore, Mick Casey, John Denton, Ivor Day, the Whittle Lab, and EPSRC for funding this work.

NOMENCLATURE

c	chord
t	blade max thickness
h	blade span
A	annulus area
DF	Lieblein's diffusion factor
p	pressure
T	temperature
R	specific gas constant
U	blade speed
$\dot{m}$	mass flow rate
V_x	axial velocity
V	relative blade inlet velocity
Re_c	Reynolds number based on chord (= $\rho V c/\mu$)
Re_h	Reynolds number based on span (= $\rho V h/\mu$)
AR	aspect ratio (= h/c)
Δh_0	change in specific stagnation enthalpy
M_b	non-dimensional blade speed (= $U/\sqrt{\gamma R T_0}$)
Δs	change in specific entropy
y	circumferential distance
r	radius

Greek letters

ε	cantilever/shroud clearance
ρ	density
μ	dynamic viscosity
ψ'	static pressure rise coefficient (= $2\Delta p/\rho U^2$)
δ^*	total endwall blockage
ϕ	flow coefficient (= V_x/U)
Δh_0	change in specific stagnation enthalpy
ψ	work coefficient (= $\Delta h_0/U^2$)
Λ	reaction
ω_p	profile loss coefficient
ω_{ew}	endwall loss coefficient
ω_t	total loss coefficient
η	isentropic efficiency

Subscripts

0	stagnation
d	design
fs	freestream

ew	endwall
b	blade-row
eff	effective
opt	optimum

Abbreviations

config	endwall configuration (i.e. shroud or cantilever)
LE	leading edge
TE	trailing edge
BL	boundary layer
HP	high pressure

REFERENCES

[1] Smith, L. H., 1970, "Casing Boundary Layers in Multistage Axial-Flow Compressors," *Flow Research on Blading*, Vol. 106, pp. 635-647

[2] Wennerstrom, A. J., 1989, "Low Aspect Ratio Axial Flow Compressors: Why and What It Means," *Journal of Turbomachinery*, Vol. 111, pp. 357-365.

[3] McKenzie, A. B., 1997, "Axial Flow Fans and Compressors," Ashgate Publishing Limited.

[4] Koch, C. C., 1981, "Stalling Pressure Rise Capability of Axial Flow Compressor Stages," *Journal of Engineering for Gas Turbines and Power*, Vol. 103(4), pp. 645-656

[5] Spalart, P. R. & Allmaras, S. R., 1992, "A One-Equation Turbulence Model for Aerodynamic Flows," AIAA Paper 92-0439

[6] Wellborn, S. R., & Okiishi, T. H., 1999, "The Influence of Shrouded Cavity Flows on Multistage Compressor Performance," *Journal of Turbomachinery*, Vol. 121, pp. 486-497

[7] Freeman, C., 1985, "Effect of tip clearance flow on compressor stability and engine performance," VKI for Fluid Dynamics Lecture Series 5

[8] Drela, M., 1986, "Two-Dimensional Transonic Aerodynamic Design and Analysis Using the Euler Equations," PhD Thesis, Massachusetts Institute of Technology

[9] Wright, P. I., & Miller, D.C., 1991, "An Improved Compressor Performance Prediction Model," *European Conference of Turbomachinery: Latest Developments in a Changing Scene*, C423/028. IMechE, 1991.

[10] Goodhand, M. N., & Miller, R., J., 2012, "The Impact of Real Geometries on Three-Dimensional Separations in Compressors," *Journal of Turbomachinery*, Vol. 134(2)

Table 1: Specification of datum & optimum design

	Datum	Optimum
Config.	Shroud	Cantilever
Design ϕ	0.550	0.550
Design ψ'	0.809	0.812
AR	0.86	1.16
ϵ/c	1%	1.35%
t/c	4.1%	5.4%
Re	6.3×10^5	4.7×10^5
$\Delta\eta_{CFD}$	-	+0.59%
$\Delta\eta_{model}$	-	+0.57%

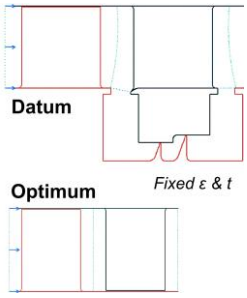

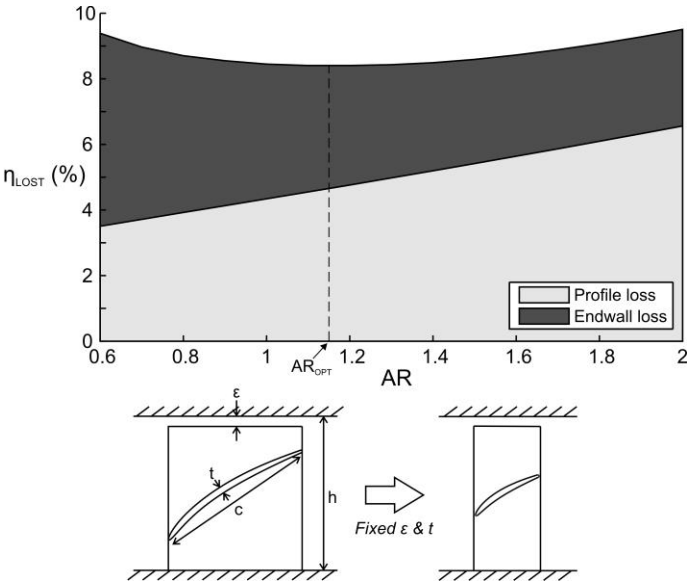

Fig. 1: Variation in lost efficiency with aspect ratio (fixed thickness & clearance)

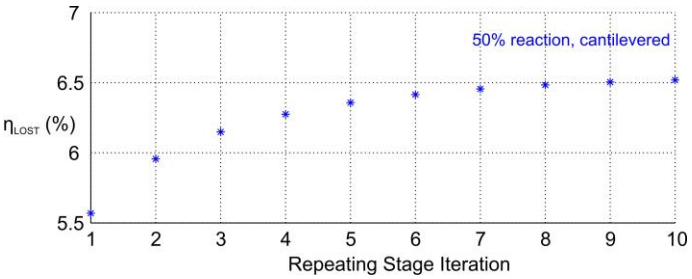

Fig. 2: Lost efficiency vs no. of repeating stage iterations (AR = 1.7, ε/c = 1.0%, t/c = 4.1%, Re_c = 6.3x10^5)

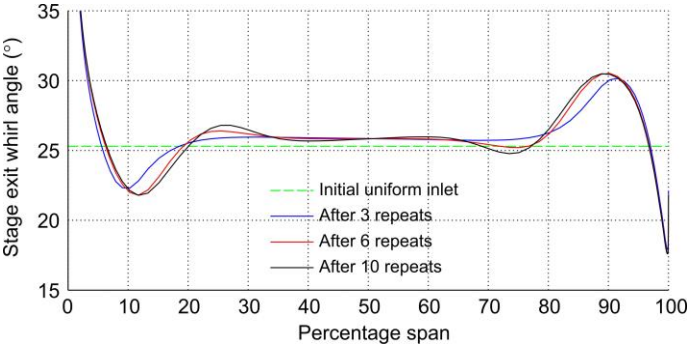

Fig. 3: Spanwise distribution of stage exit whirl angle after different no. of repeats (AR, ε/c, t/c, Re_c as above)

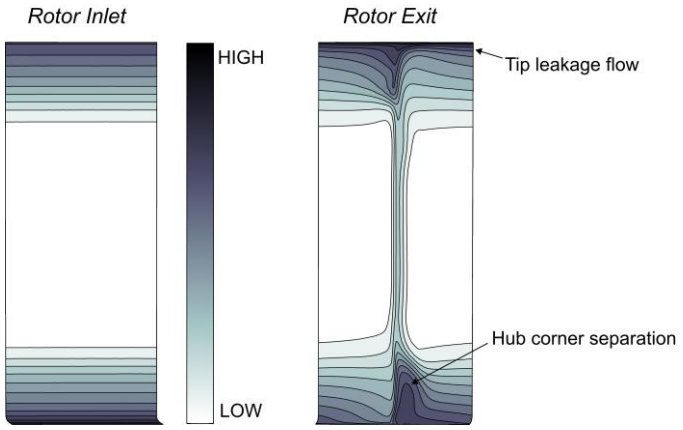

Fig. 4: Entropy contours (note use of mixing planes)

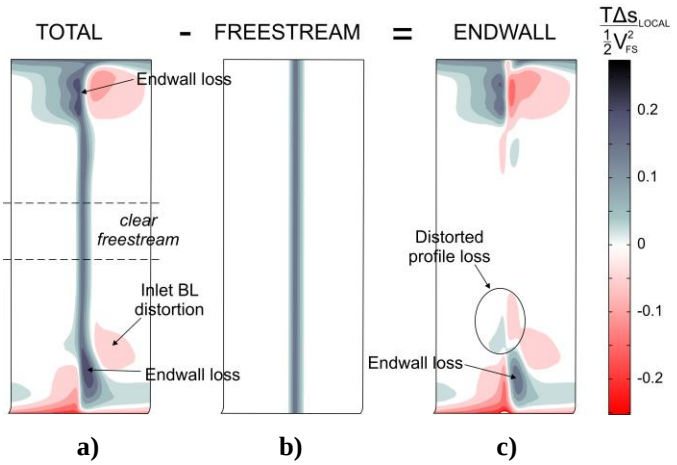

Fig. 5: Flow decomposition; clear freestream (AR=1.7)

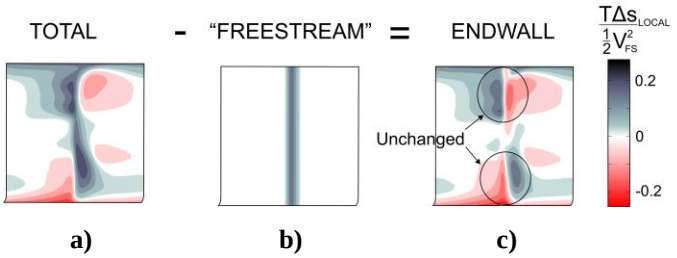

Fig. 6: Flow decomposition; no clear freestream (AR=0.7)

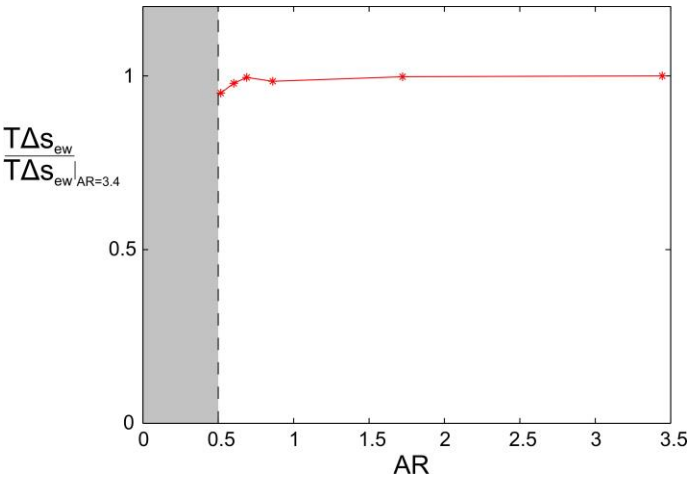

Fig. 7: Entropy generation due to endwalls vs. AR (ε/c = 2.0%, t/c = 4.1%, Re_c = 6.3x10^5)

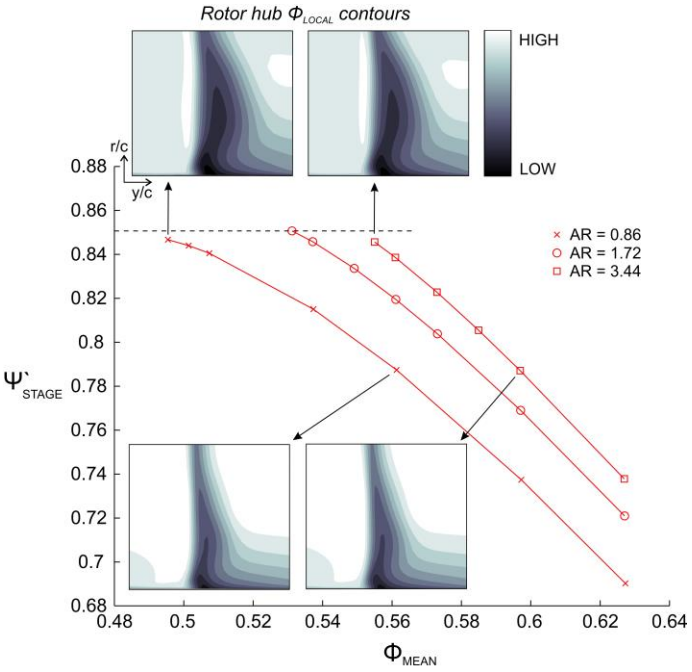

Fig. 8: Dependence of endwall flow on pressure rise coefficient (& independence of AR)

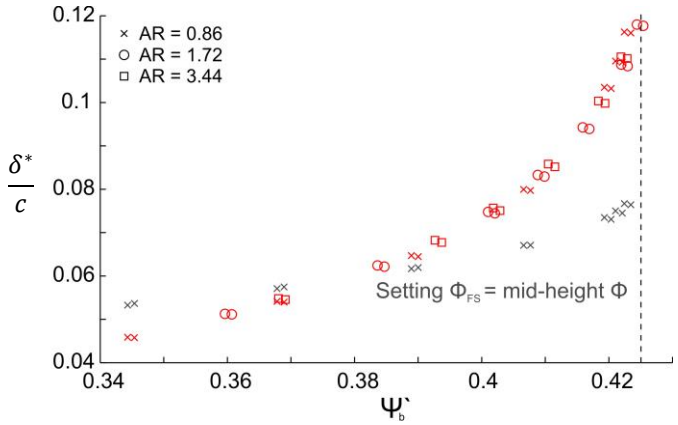

Fig. 9: Blockage-to-chord dependence on pressure rise coefficient (& independence of AR)

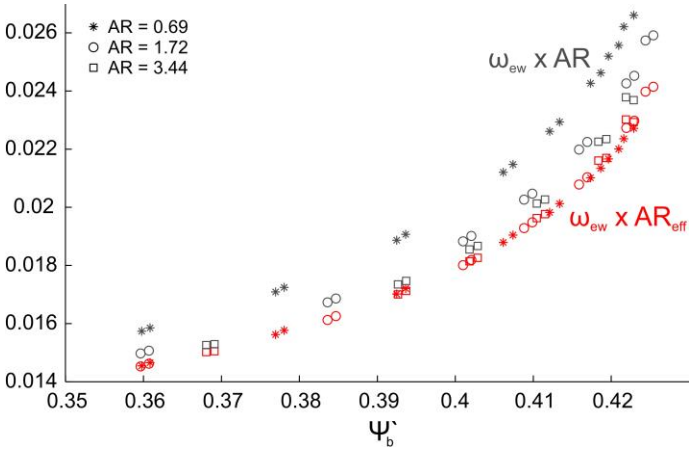

Fig. 10: Endwall loss varies inversely with effective AR and not AR (ε/c = 1.0%)

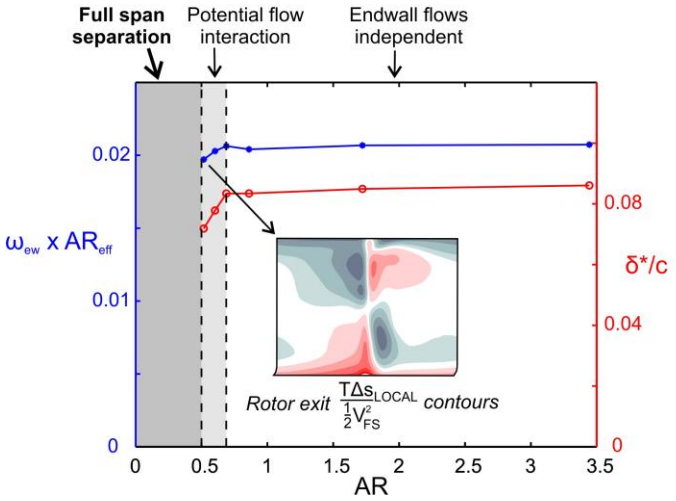

Fig. 11: Endwall loss & blockage vs. AR (ε/c = 2.0%, t/c = 4.1%, Re_c = 6.3x10^5)

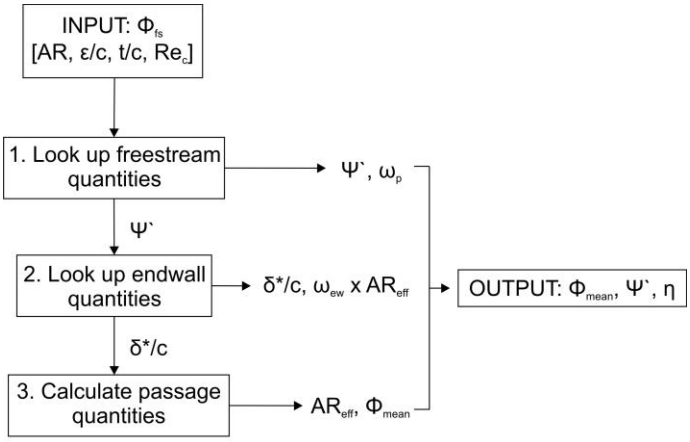

Fig. 12: Low order model structure

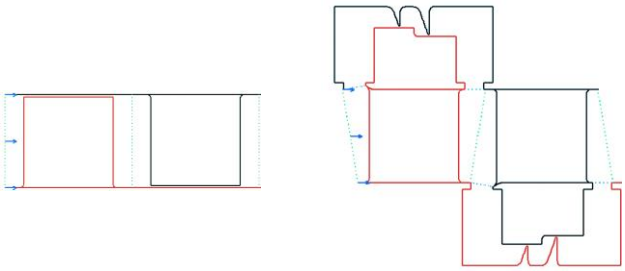

a) Cantilevered **b) Shrouded**

Fig. 13: Endwall configuration used to decouple effects

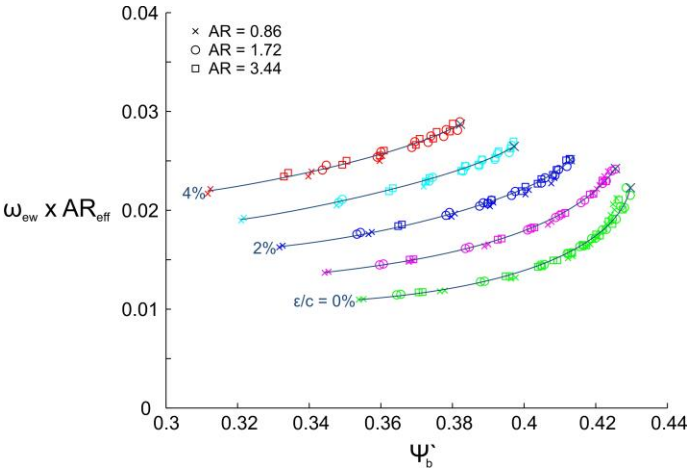

Fig. 14: Variation in endwall loss coefficient with blade-row pressure rise coefficient over characteristic (cantilevered)

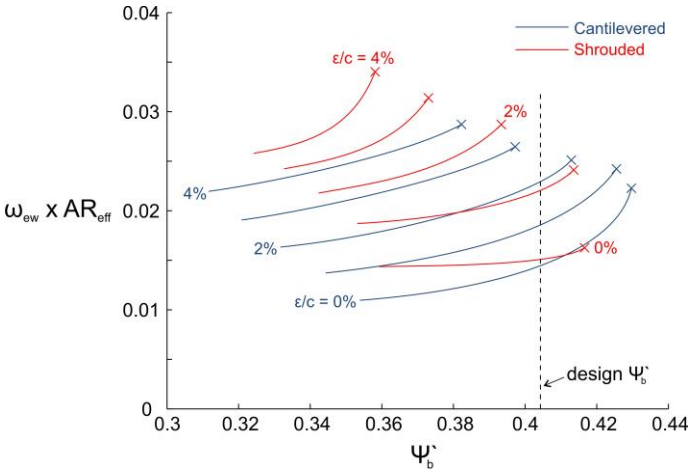

Fig. 15: Comparison of endwall loss coefficient for cantilevered & shrouded endwalls

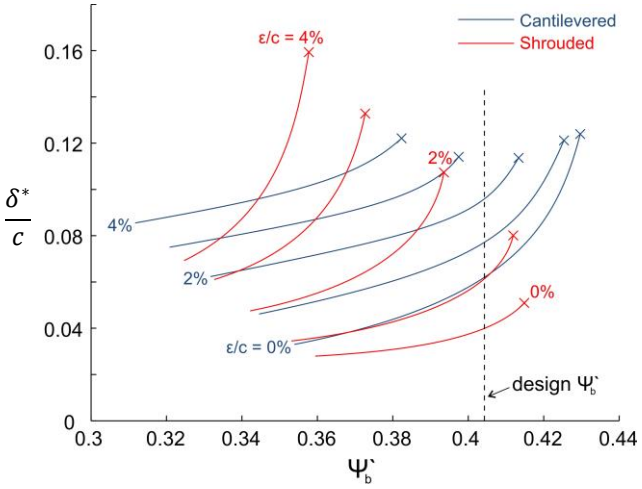

Fig. 16: Comparison of blockage for cantilevered & shrouded endwalls

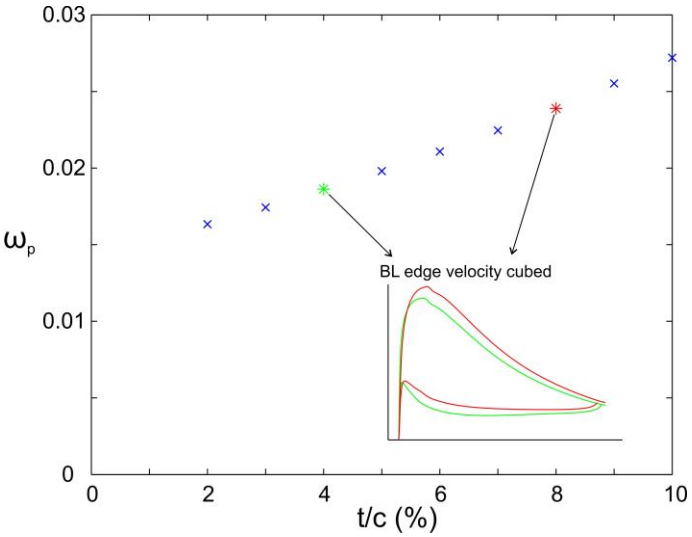

Fig. 17. Profile loss variation with t/c (MISES)

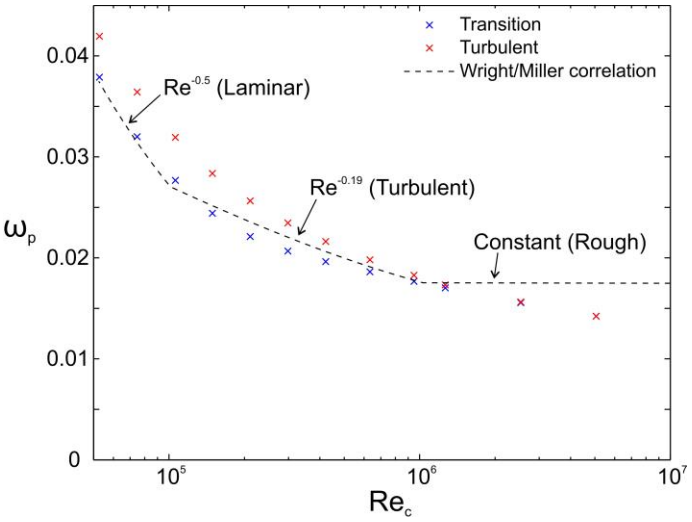

Fig. 18: Profile loss variation with Re_c (MISES)

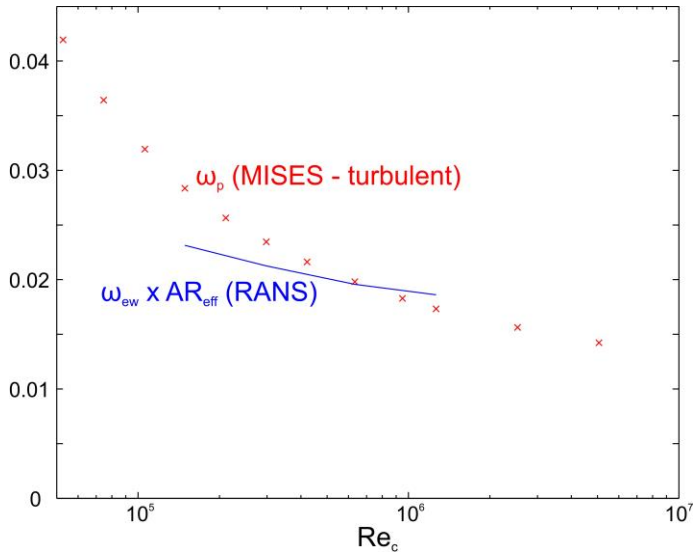

Fig. 19: Comparison of profile & endwall loss variation with Re_c (ε/c = 2.0%)

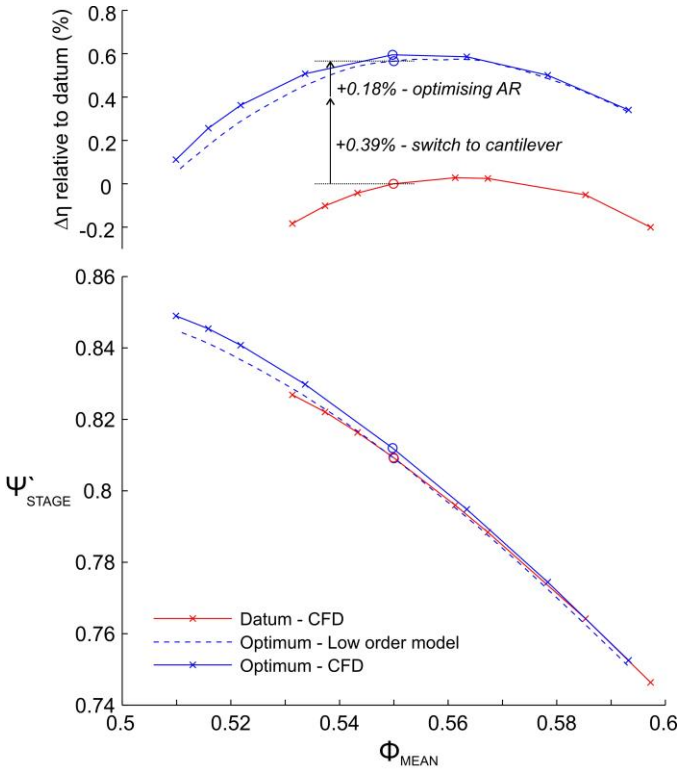

Fig. 20: Validation of low order model against CFD

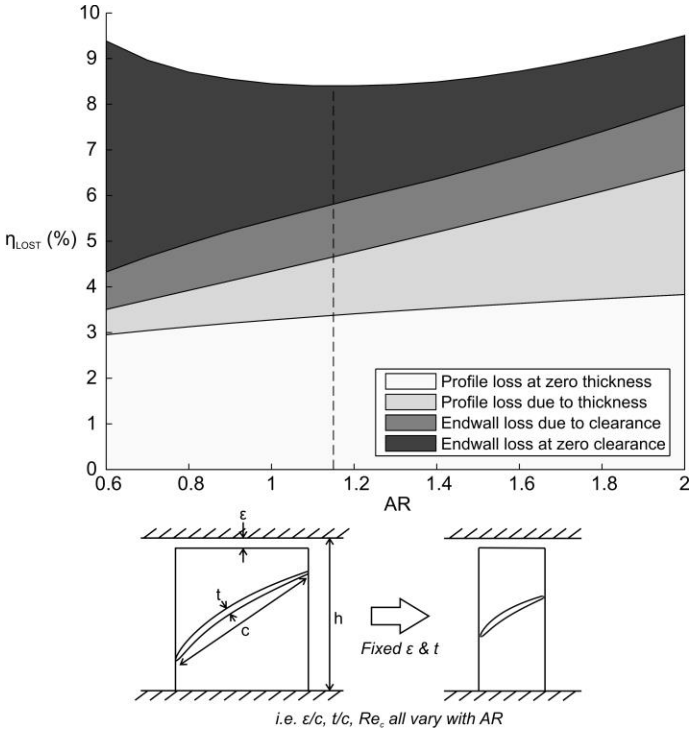

Fig. 21: Breakdown of lost efficiency using low order model (t/h = 4.7%, ε/h = 1.2%, Re_h = 5.5x10^5)

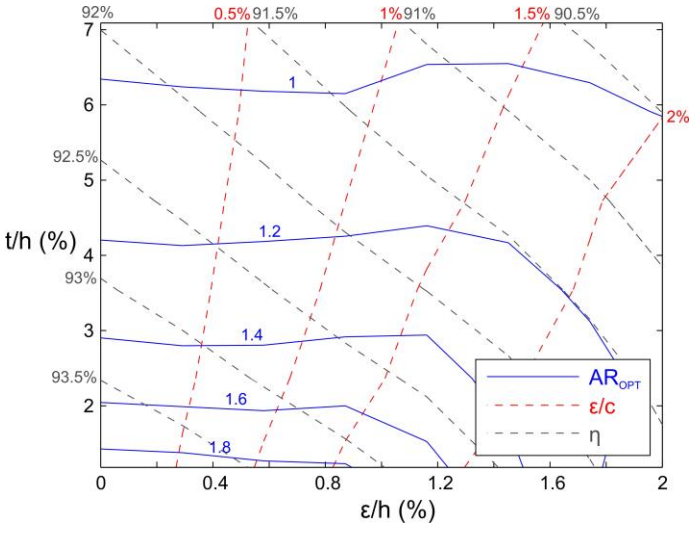

Fig. 22: Contours of optimum AR, ε/c & η (low order model, cantilevered, Re_h = 5.5x10^5)

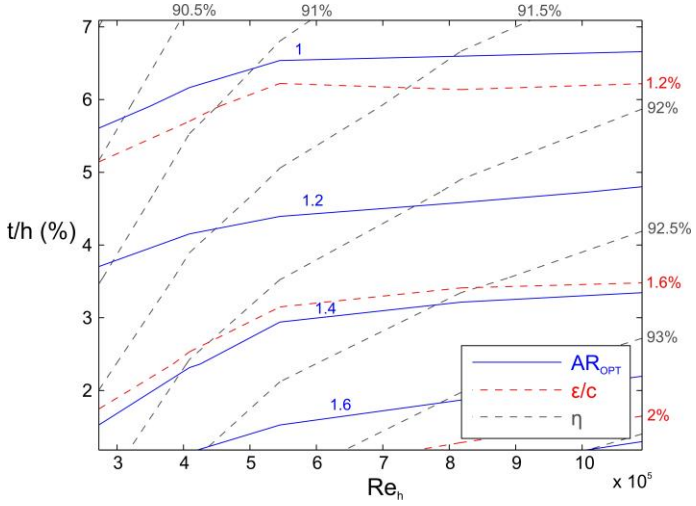

Fig. 23: Contours of optimum AR, ε/c & η (low order model, cantilevered, ε/h = 1.2%)

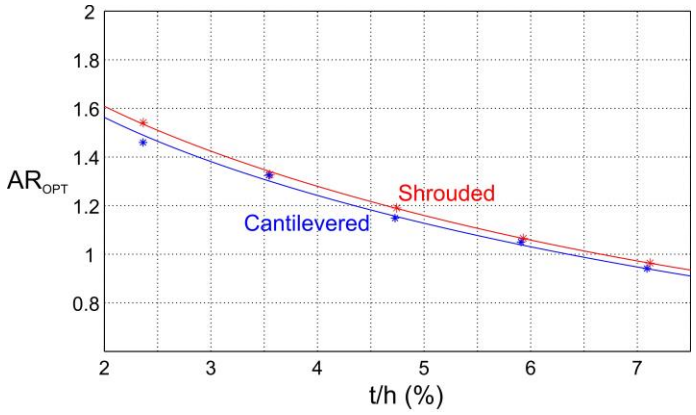

Fig. 24: Comparison of optimum AR for the endwall configurations of Fig. 13 (low order model, ε/h = 0%)

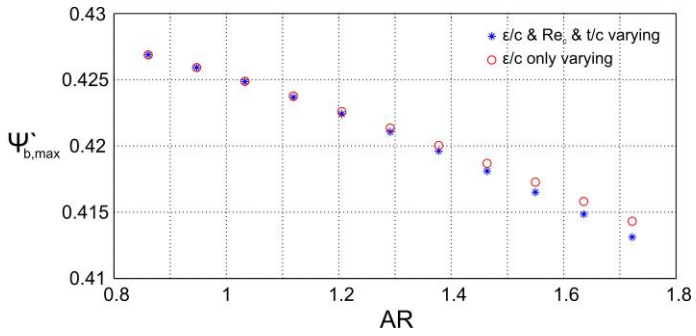

Fig. 25: The variation of max pressure rise coefficient with AR (ε/h = 4.7%, ε/h = 1.2%, Re_h = 5.5x10^5)

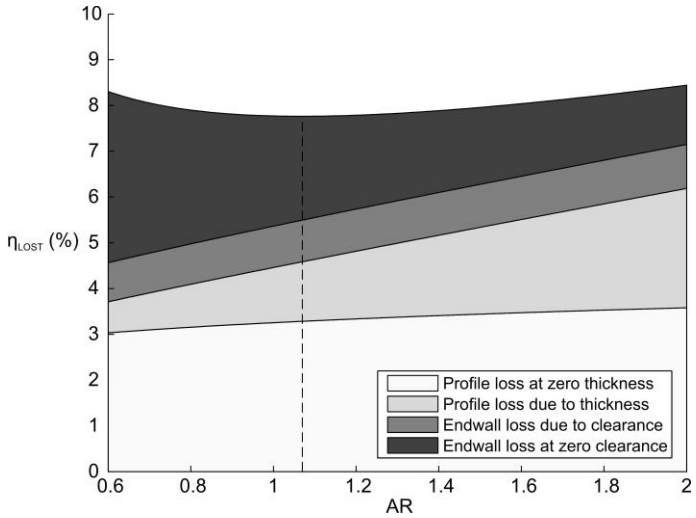

Fig. 26: Breakdown of lost efficiency using simple analytical model of Eq. (12) (t/h = 4.7%, ε/h = 1.2%, Re_h = 5.5x10^5)

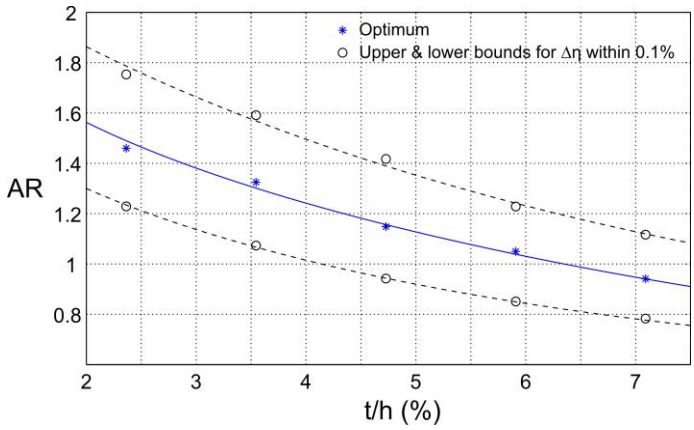

Fig. 27: AR range with efficiencies within 0.1% of optimum (low order model, cantilever, ε/h = 1.2%, Re_h = 5.5x10^5)